Title
Real-time needle guidance for venipuncture based on optical coherence tomography

Journal
Computer Methods in Biomechanics and Biomedical Engineering Imaging & Visualization, 9(6)

ISSN
2168-1163

Authors
Farouki, Rida T
Swett, Jack R
Rohlen, Rachel Ward
et al.

Publication Date
2021-11-02

DOI
10.1080/21681163.2021.1914734

Peer reviewed

Real-time needle guidance for venipuncture based on optical coherence tomography

Rida T. Farouki and Jack R. Swett
Department of Mechanical and Aerospace Engineering,
University of California, Davis, CA 95616, USA.

Rachel Ward Rohlen and David B. Smith
WestFace Medical, Redwood City, CA 94063, USA.

Abstract

An algorithm for real–time venipuncture needle guidance is described, using an optical coherence tomography (OCT) probe that emits light pulses at fixed angular intervals along a cone, giving accurate distance measurements to points on the blood vessel. Using this data, a method is developed to visually display the blood vessel for needle guidance. A least–squares fit to a general quadric surface, specified by a symmetric matrix, is performed. For a cylindrical blood vessel, this provides an estimate for its orientation, from which its location and radius can be determined. The algorithm is compatible, in efficiency and robustness, with real–time implementation.

Keywords: needle guidance; optical coherence tomography; quadric surfaces; least–squares fit; cylinder characterization.

e–mail addresses: farouki@ucdavis.edu, jrswett@ucdavis.edu, rachel@westfacemd.com, dsmith@westfacemd.com

1 Introduction

Although collection of blood samples by venipuncture is a commonplace and indispensable procedure, it has an imperfect initial success rate even among experienced medical personnel. To address this, the `SingleStick`™ device under development by WestFace Medical incorporates an optical coherence tomography (OCT) probe to provide real–time visual interactive guidance of a needle toward the blood vessel. A basic requirement in this technology is the real–time translation of discrete distance measurements from the probe to the blood vessel, at specific inclinations to the needle axis, into quantitative information concerning the position, orientation, and size of the blood vessel, so as to provide real–time visual guidance to the user.

Since its development in the early 1990s, optical coherence tomography has been extensively adopted in the context of non–invasive retinal imaging [1, 6, 7] and is being increasingly employed in other biomedical applications. A brief review of OCT is presented in Section 2 — more complete details on its historical development and applications be found in [4, 5, 10].

The `SingleStick`™ OCT probe emits a sequence of light pulses along a conical surface with a beam angle $\phi = 60^\circ$ relative to the needle axis and equidistant azimuthal spacing $\delta\theta = 0.5^\circ$ about the axis, which yield accurate distance measurements to points on the blood vessel. Several scans may be made, at successive extensions δz of the probe from the needle tip.

The blood vessel is nominally modeled as a cylindrical surface, and since the discrete point data determined by the OCT probe are of finite accuracy, a least–squares approach to identifying the cylinder is desirable to suppress the influence of measurement noise. A cylinder is uniquely identified by its axis, radius, and a point on the axis. However, the implicit equation $f(x, y, z) = 0$ expressed in terms of these intuitive parameters has a non–linear dependence on them, necessitating the use of an iterative solution procedure which may be incompatible with real–time computation, or fail to converge when reliable starting approximations cannot be determined *a priori*.

To circumvent these problems, the approach adopted herein is to perform a least–squares fit of the data points to a general quadric surface, resulting in a *linear* system of equations for the unknown coefficients. These coefficients may be regarded as the elements of a symmetric 4×4 matrix, and an analysis of the eigenvalues and eigenvectors of this matrix allows the "best" cylinder fit to be identified in a consistently efficient and robust manner.

The remainder of this paper is organized as follows. Section 2 reviews the basic principles of optical coherence tomography and their application to the real–time needle guidance problem. The representations of quadric surfaces in terms of 4×4 real symmetric matrices is then introduced in Section 3, and cylinders are identified in terms of invariants and the matrix eigenvalues. In Section 4 we discuss the relative merits of equations that describe cylinders explicitly in terms of their geometrical parameters or as general quadrics in the least–squares surface fit problem, and the need for multiple OCT scans to ensure unambiguous cylinder identifications. The formulation and solution of the least–squares fitting procedure, based upon the general quadric equation, is treated in Section 5, and in Section 6 we describe the determination of the cylinder axis and radius from the computed quadric surface coefficients. In Section 7 we assess the accuracy of the cylinder identification, in view of the limited precision of the OCT distance measurements. Section 8 then presents some computed examples to illustrate the performance of the algorithm, and Section 9 discusses the feasibility of its real–time implementation. Finally, in Section 10 we summarize the main results of this study, and identify aspects that deserve further investigation.

2 Optical coherence tomography

Optical coherence tomography (OCT) is an imaging modality, analogous to ultrasound, that uses low–coherence interferometry to obtain high–resolution 3D images of biological tissue at depths of a few mm [8]. A broad–spectrum light source in the near infrared or infrared band is used to optimize depth of penetration, with the light being transmitted from the end of a fiber optic line. Although most of the light is lost by absorption or multiple scattering, a small fraction (10^{-6}–10^{-9}) will be scattered by a single tissue feature, and travels back along the fiber to an interferometer that uses coherent detection (constructive/destructive interference of transmitted and returned signals) to obtain image resolution $< 10\,\mu$m over depths of 1–2 mm.

Since the light signal round–trip time–of–flight is too short to accurately measure, the data are transformed into the distance or the frequency domain. The original OCT implementation, known as Time Domain (TD) OCT, was based on inteference of signals from the sample and a reference arm mirror. However, the need for rapid, accurate, and repeatable mirror movemement limits the resolution achievable through TD OCT. Swept Source (SS) OCT is a contemporary Fourier Domain (FD) technology that provides substantial improvements in signal acquisition rates and signal–to–noise ratios. SS OCT employs a chirped (i.e., rapid wavelength swept) laser light source and Fast Fourier Transform (FFT) analysis to transform the data from amplitude vs. frequency to intensity vs. depth. Spectral Domain (SD) OCT is another FD OCT variant that provides substantial improvements in both sampling rates and signal–to–noise ratio over TD OCT.

Regardless of method, the OCT system returns a 1–dimensional array of tissue reflectivity as a function of incremental depth. This array is referred to as an "A–line." Multiple A–lines can be aggregated as a "B-scan" defining a raster scan in either Cartesian (x, y) or polar (r, θ) coordinates. A–lines can also be assembled left–to–right as a function of time, yielding a "waterfall" diagram that represents reflectivity along a particular vector in the tissue as a function of both depth and time (this format is useful in studying temporal variations). In our implementation, the OCT probe is rotated as a function of time, and angle data is reconstructed from time stamps. The B–scan indices are then interpreted as polar coordinates to create a "radar" plot.

Various signal processing methods can be applied to the A–lines or B–scans to generate tissue images or extract information useful for diagnostic or procedural purposes. In the context of the `SingleStick`™ needle guidance problem, the goal is to identify the instantaneous position and orientation of a blood vessel relative to the needle tip, via a surface reconstruction problem in B–Scan space. A distinctive feature of the `SingleStick`™ technology is the real–time collection and interpretation of OCT data for navigation and therapeutic purposes, based on a proprietary method for steering the needle to the blood vessel (contemporary OCT is most frequently used in a post–processing workflow — i.e., the imaging data is collected and then analyzed off–line for presentation in a diagnostic context).

Although the blood vessel identification algorithm described herein was motivated by a particular OCT application, it is not restricted to OCT. Any imaging modality that can reconstruct a list of surface detection events may — assuming sufficient resolution — benefit from the algorithm.

3 General quadric surfaces

The data generated by the OCT probe correspond to a discrete sampling of points on the intersection curve of an indeterminate cylinder with a known cone. The problem is to determine the position, orientation, and radius of the cylinder from these data points. Cylinders and cones[1] are special instances of the entire family of algebraic surfaces of degree 2, the *quadric surfaces*.

The characterization of quadric surfaces is a fundamental topic in classical algebraic geometry [2, 11, 12]. The implicit equation of a general quadric may be specified in terms of a symmetric 4×4 matrix through the expression

$$q(x,y,z) \;=\; [\; x \;\; y \;\; z \;\; 1 \;] \begin{bmatrix} a & f & h & l \\ f & b & g & m \\ h & g & c & n \\ l & m & n & d \end{bmatrix} \begin{bmatrix} x \\ y \\ z \\ 1 \end{bmatrix} \;=\; 0\,.$$

Expanding the matrix product gives

$$ax^2 + by^2 + cz^2 + 2fxy + 2gyz + 2hzx + 2lx + 2my + 2nz + d \;=\; 0\,. \tag{1}$$

The eigenvectors of the upper–left 3×3 sub–matrix

$$\begin{bmatrix} a & f & h \\ f & b & g \\ h & g & c \end{bmatrix} \tag{2}$$

determine the *principal axes* of the quadric surface. The eigenvalues are the roots ξ of the characteristic equation

$$\xi^3 - \beta\,\xi^2 + \gamma\,\xi - \delta \;=\; 0\,, \tag{3}$$

with coefficients

$$\beta \;:=\; a + b + c\,, \quad \gamma \;:=\; ab + bc + ca - f^2 - g^2 - h^2\,, \tag{4}$$

$$\delta \;:=\; abc + 2fgh - ag^2 - bh^2 - cf^2\,. \tag{5}$$

Since the matrix (2) is symmetric, its eigenvalues are all real. The quantities β, γ, δ — together with the determinant

$$\Delta \;:=\; \begin{vmatrix} a & f & h & l \\ f & b & g & m \\ h & g & c & n \\ l & m & n & d \end{vmatrix}$$

[1]Henceforth, "cylinder" and "cone" refer exclusively to *right circular* cylinders and cones, whose sections by any plane orthogonal to their axes is a circle.

of the 4×4 matrix — are *invariants* [11] of the quadric surface: they remain unchanged under a motion (translation/rotation) of the surface.

The cones and cylinders are *ruled* quadric surfaces, generated by a one–parameter family of lines. For a cone, these lines pass through a fixed point (the *vertex*), and maintain a constant angle with a fixed line (the *axis*). For a cylinder, the lines are parallel to and equidistant from a fixed line (the *axis*). The cylinder may be regarded as a special instance of the cone, with a *point at infinity* as the vertex, and we refer to the set of all cones and cylinders as *generalized cones*. The generalized cones are *singular* quadrics, distinguished by the condition $\Delta = 0$. In terms of the other invariants, a cone is identified by the condition $\delta \neq 0$, and a cylinder is identified by $\delta = 0$, $\gamma \neq 0$. These conditions identify all (not just right circular) cones and cylinders.

With $\delta = 0 \neq \gamma$ equation (3) reduces, on factoring out the root $\xi = 0$, to

$$\xi^2 - \beta\,\xi + \gamma \;=\; 0\,,$$

and a right circular cylinder is identified by the condition, $\beta^2 - 4\,\gamma = 0$, that this quadratic equation should have a double root — namely, $\xi = \frac{1}{2}\beta$.

4 Cylinders as quadric surfaces

A cylinder of general position and orientation may be specified by its radius r, a point $\mathbf{p}_* = (x_*, y_*, z_*)$ on its axis, and a unit vector $\mathbf{a} = (\lambda, \mu, \nu)$ satisfying

$$\lambda^2 + \mu^2 + \nu^2 \;=\; 1\,, \tag{6}$$

that defines the axis orientation. The implicit equation of the cylinder may be written explicitly in terms of these geometrical parameters as follows.

The position of a general point $\mathbf{p} = (x, y, z)$ relative to $\mathbf{p}_*$ can be resolved into components parallel and perpendicular to the axis $\mathbf{a}$ as

$$\mathbf{p} - \mathbf{p}_* \;=\; [\,(\mathbf{p} - \mathbf{p}_*) \cdot \mathbf{a}\,]\,\mathbf{a} + \mathbf{a} \times [\,(\mathbf{p} - \mathbf{p}_*) \times \mathbf{a}\,]\,.$$

The equation of the cylinder is then determined from the condition that the perpendicular distance of $\mathbf{p}$ from the axis is r, and this reduces to

$$|\,\mathbf{a} \times (\mathbf{p} - \mathbf{p}_*)\,|^2 \;=\; r^2\,. \tag{7}$$

Expressing this in terms of the coordinates of $\mathbf{p}$, and making use of (6), we obtain the implicit equation

$$\begin{aligned} f(x,y,z) \;=\; & (1-\lambda^2)(x-x_*)^2 - \, 2\,\lambda\mu\,(x-x_*)(y-y_*) \\ +\; & (1-\mu^2)(y-y_*)^2 - 2\,\mu\nu\,(y-y_*)(z-z_*) \\ +\; & (1-\nu^2)(z-z_*)^2 - 2\,\nu\lambda\,(z-z_*)(x-x_*) - r^2 \;=\; 0\,. \end{aligned} \tag{8}$$

Note that this equation is invariant upon replacing (x_*,y_*,z_*) by $(x_*,y_*,z_*)+\alpha\,(\lambda,\mu,\nu)$ for any α — i.e., it does not depend on the choice of the point $\mathbf{p}_*$ on the cylinder axis. In the present context, we may assume that $z_* = 0$ (this is valid if $\nu \neq 0$, i.e., the cylinder axis is not parallel to the (x,y) plane).

The form (8) corresponds to coefficients in the general quadric equation (1) specified by

$$(a,b,c) \;=\; (1-\lambda^2, 1-\mu^2, 1-\nu^2)\,, \quad (f,g,h) \;=\; (-\,\lambda\mu, -\,\mu\nu, -\,\nu\lambda)\,, \tag{9}$$

$$(l,m,n) \;=\; (-\,a\,x_* - f\,y_* - h\,z_*, -f\,x_* - \,b\,y_* - g\,z_*, -h\,x_* - g\,y_* - \,c\,z_*)\,, \tag{10}$$

$$d \;=\; a\,x_*^2 + b\,y_*^2 + c\,z_*^2 + 2\,f\,x_*y_* + 2\,g\,y_*z_* + 2\,h\,z_*x_* - r^2\,, \tag{11}$$

where it is understood that the constraint (6) also holds.

In principle, a quadric surface can be uniquely determined from 9 points lying in "general position" on it, since equation (1) depends on 10 coefficients, and the surface is unchanged upon dividing (1) by any non–zero coefficient. However, since the 9 points must be exactly specified, and verifying that they are in "general position" is non–trivial, this approach is impractical.

Given N data points $\mathbf{p}_i = (x_i,y_i,z_i)$, $i = 1,\ldots,N$ on the intersection of a known cone and a cylinder, we wish to determine the cylinder. Since the data will be subject to measurement noise, a least–squares fitting scheme is desirable to suppress the influence of the noise. The least–squares fit may be based on either the general quadric surface equation (1), or the equation (8) expressed in terms of the cylinder geometrical parameters.

Equation (8) explicitly determines a cylinder in terms of the geometrical parameters $\mathbf{p}_*, \mathbf{a}, r$. However, the dependence upon these parameters is not linear, and the least–squares fit will incur a constrained system of *non–linear* equations. A computationally–intensive iterative method is required to solve this system, and without a reliable scheme for choosing "good" starting values it will not be sufficiently robust for real–time implementation.

Equation (1), on the other hand, is linear in the coefficients $a, b, c, \ldots$ and the least–squares fit incurs a system of *linear* equations for these unknowns, that has a unique solution (if the matrix defined by equations (13)–(15) below is non–singular). Since the general quadric equation (1) does not explicitly determine the least–squares fit surface as a cylinder, the geometry parameters $\mathbf{p}_*, \mathbf{a}, r$ of the "nearest" true cylinder must be extracted from the computed coefficients $a, b, c, \ldots$, as described in Section 6.

In view of the above considerations, equation (1) will be employed in the least–squares surface fit. As observed above, the OCT scan identifies points on the intersection curve of a known cone with the unknown cylinder. This amounts to a one–dimensional sampling of a two–dimensional surface that is, in general, insufficient to uniquely identify the surface. Two or more scans, at different extensions δz of the probe along the needle axis, are required.

This may be seen as follows. The intersection of two quadric surfaces $q_0(x, y, z) = 0$ and $q_1(x, y, z) = 0$ is, in general, an *irreducible quartic space curve*[2] [11]. There are infinitely–many pairs of quadric surfaces that possess the same intersection curve C as $q_0(x, y, z) = 0$ and $q_1(x, y, z) = 0$. Any two members of the *pencil of quadrics* defined by

$$q_\tau(x, y, z) \,=\, (1-\tau)\, q_0(x, y, z) + \tau\, q_1(x, y, z) \,=\, 0\,, \quad -\infty < \tau < +\infty$$

corresponding to distinct τ values possess the same intersection curve C as $q_0(x, y, z) = 0$ and $q_1(x, y, z) = 0$. Thus, given one of two quadrics, it is not possible to uniquely identify the other from their intersection curve.

In the present context, one quadric is a known cone, and we can exploit the additional information that the unknown quadric is a cylinder. Suppose $\mathbf{Q}_0$ and $\mathbf{Q}_1$ are symmetric 4×4 matrices with elements $a_0, b_0, \ldots$ and $a_1, b_1, \ldots$, specifying two quadric surfaces. Then the determinantal equation

$$p(\tau) \,=\, |\, (1-\tau)\, \mathbf{Q}_0 \,+\, \tau\, \mathbf{Q}_1 \,| \,=\, 0$$

is of degree 4, and its (real) roots identify the *generalized cones* of the pencil defined by $\mathbf{Q}_0$ and $\mathbf{Q}_1$. The quartic polynomial $p(\tau)$ is called the *discriminant* [11] of the pencil of quadrics. In the generic case, in which the roots of $p(\tau)$ are distinct, the intersection C is a non–singular quartic space curve [3].

To verify that a cylinder $\mathbf{Q}_1$ constructed from a known intersection curve C with a known cone $\mathbf{Q}_0$ is unique, we must determine the real roots of the

[2] It may degenerate into a collection of simpler curves (lines, conics, and cubics) whose degrees sum to 4.

discriminant $p(\tau)$ of the pencil defined by $\mathbf{Q}_0$ and $\mathbf{Q}_1$, and check that none of the quadrics corresponding to these roots (other than $\tau = 1$) is a cylinder. Ferrari's method [13] provides a closed–form solution for all the roots of $p(\tau)$. This uniqueness test can only be performed *a posteriori* — i.e., after $\mathbf{Q}_1$ has been constructed. However, using multiple scans at successive extensions δz of the OCT probe eliminates the need to perform this test.

5 Least-squares fit procedure

Equation (1) may be divided by any non–zero coefficient without influencing the quadric surface it defines. In the present context, we may divide through by d, which corresponds to the choice $d = 1$ in (1). This is permissible if the surface $q(x, y, z) = 0$ does not pass through the origin, which is true since the origin is defined to be the apex of the cone (i.e., the position of the sensor) and the sensor does not encroach on the cylinder.

We adopt a coordinate system in which the needle axis is identified with the z–axis, and for zero extension the OCT probe is located at $z = 0$. The known parameters and available data are the cone beam angle ϕ about the z–axis, the measured distances ρ_i from the probe to the blood vessel surface, and the associated azimuthal angles θ_i on the cone and probe extensions δz_i for each measured point, $i = 1, \ldots, N$. For the least–squares fit, the data are converted to Cartesian coordinates according to

$$x_i \,=\, \rho_i \sin\phi \sin\theta_i \,, \quad y_i \,=\, \rho_i \sin\phi \cos\theta_i \,, \quad z_i \,=\, \rho_i \cos\phi + \delta z_i \,. \tag{12}$$

With $d = 1$, the remaining unknown 9 coefficients $a, b, c, f, g, h, l, m, n$ in (1) are determined by minimizing the expression

$$E \,=\, \sum_{i=1}^{N} q^2(x_i, y_i, z_i) \,.$$

Setting the partial derivatives of E with respect to these coefficients equal to zero results in a linear system of equations of the form

$$\mathbf{M}\,\mathbf{v} \,=\, \mathbf{r} \,, \tag{13}$$

where $\mathbf{v} = [\, a\ b\ c\ f\ g\ h\ l\ m\ n\,]^T$ and, on introducing the basis functions

$$\begin{gathered} \phi_1(x,y,z) \,=\, x^2 \,, \quad \phi_2(x,y,z) \,=\, y^2 \,, \quad \phi_3(x,y,z) \,=\, z^2 \,, \\ \phi_4(x,y,z) \,=\, 2\,xy \,, \quad \phi_5(x,y,z) \,=\, 2\,yz \,, \quad \phi_6(x,y,z) \,=\, 2\,zx \,, \\ \phi_7(x,y,z) \,=\, 2\,x \,, \quad \phi_8(x,y,z) \,=\, 2\,y \,, \quad \phi_9(x,y,z) \,=\, 2\,z \,, \end{gathered} \tag{14}$$

the elements of the matrix $\mathbf{M}$ and right–hand side vector $\mathbf{r}$ can be expressed in terms of the data points (x_i, y_i, z_i) as

$$M_{jk} \;=\; \sum_{i=1}^{N} \phi_j(x_i, y_i, z_i)\, \phi_k(x_i, y_i, z_i)\,, \quad 1 \le j, k \le 9\,, \tag{15}$$

$$r_j \;=\; -\sum_{i=1}^{N} \phi_j(x_i, y_i, z_i)\,, \quad 1 \le j \le 9\,. \tag{16}$$

The linear system (13) has a unique solution when $\mathbf{M}$ is non–singular, which can be efficiently computed by Gaussian elimination.

6 Cylinder geometry parameters

Once the vales $a, b, c, f, g, h, l, m, n$ have been computed, we must obtain the cylinder geometrical parameters $\mathbf{p}_*, \mathbf{a}, r$ from them. The *principal axes* of the quadric surface are identified by the eigenvectors (v_x, v_y, v_z) of the 3×3 matrix (2) — i.e., by the solutions of the equation

$$\begin{bmatrix} a-\xi & f & h \\ f & b-\xi & g \\ h & g & c-\xi \end{bmatrix} \begin{bmatrix} v_x \\ v_y \\ v_z \end{bmatrix} = \begin{bmatrix} 0 \\ 0 \\ 0 \end{bmatrix}, \tag{17}$$

where the eigenvalues ξ are the roots of the characteristic equation (3) with the coefficients (4)–(5). As observed in Section 3, for an exact right circular cylinder $\xi = 0$ is one eigenvalue (with no valid associated eigenvector), and $\xi = \frac{1}{2}\beta$ is a double eigenvalue, with which we may associate two linearly–independent eigenvectors. The latter eigenvectors span a *diametral plane* of the cylinder, orthogonal to its axis. Hence, the three row vectors of the 3×3 matrix in (17) must be parallel (or anti–parallel) to the cylinder axis.

If the coefficients a, b, c, f, g, h are determined from a least–squares fit to noisy data, they will not exactly define a right circular cylinder, and the row vectors of the 3×3 matrix in (17) will not be precisely parallel or antiparallel. To estimate the cylinder axis, we form the three unit vectors

$$\mathbf{u}_1 \;=\; \frac{(a-\xi, f, h)}{|\,(a-\xi, f, h)\,|}\,, \quad \mathbf{u}_2 \;=\; \frac{(f, b-\xi, g)}{|\,(f, b-\xi, g)\,|}\,, \quad \mathbf{u}_3 \;=\; \frac{(h, g, c-\xi)}{|\,(h, g, c-\xi)\,|}$$

and, taking $\mathbf{u}_1$ as a reference, we reverse $\mathbf{u}_2$ if $\mathbf{u}_1 \cdot \mathbf{u}_2 < 0$ and $\mathbf{u}_3$ if $\mathbf{u}_1 \cdot \mathbf{u}_3 < 0$. The cylinder axis $\mathbf{a}$ is then estimated as the centroid of these unit vectors, namely

$$\mathbf{a} \,=\, \frac{\mathbf{u}_1 + \mathbf{u}_2 + \mathbf{u}_3}{|\,\mathbf{u}_1 + \mathbf{u}_2 + \mathbf{u}_3\,|}\,. \tag{18}$$

Consider next the determination of the point $\mathbf{p}_* = (x_*, y_*, z_*)$ on the axis. As previously noted, we may assume that $z_* = 0$ if the cylinder axis is not parallel to the (x, y) plane. With $d = 1$, the restriction of (1) to the plane $z = 0$ identifies a conic curve specified by the equation

$$ax^2 + by^2 + 2fxy + 2lx + 2my + 1 \,=\, 0\,. \tag{19}$$

Provided that $ab - f^2 \neq 0$, this defines a *central conic*, and its center identifies the intersection of the cylinder axis with the (x, y) plane. The center can be determined by identifying the shift $(x, y) \to (x + x_*, y + y_*)$ of the origin that will eliminate the terms of (19) linear in x and y. One can easily verify that

$$(x_*, y_*) \,=\, \left(\frac{fm - lb}{ab - f^2}, \frac{fl - ma}{ab - f^2} \right)\,. \tag{20}$$

The final parameter to be determined is the cylinder radius r. Knowing the cylinder axis $\mathbf{a}$ and a point $\mathbf{p}_*$ on it, a robust approach is to compute r as the root–mean–square distance of the N data points $\mathbf{p}_i = (x_i, y_i, z_i)$ from the cylinder axis. Thus, based on equation (7), the radius is estimated as

$$r \,=\, \left[\, \frac{1}{N} \sum_{i=1}^{N} |\,(\mathbf{p}_i - \mathbf{p}_*) \times \mathbf{a}\,|^2 \,\right]^{1/2}\,. \tag{21}$$

For a quadric surface defined by equation (1) that is a true right circular cylinder, and *exact* data points $\mathbf{p}_1, \ldots, \mathbf{p}_N$, the above procedure can precisely identify its geometry parameters. First, with the eigenvalue $\xi = \frac{1}{2}(a + b + c)$, the rows of the of the 3×3 matrix in (17) will be precisely linearly dependent, and unitizing any of them will exactly determine the axis vector $\mathbf{a}$. Moreover, the point $\mathbf{p}_* = (x_*, y_*, z_*)$ on the axis with $z_* = 0$ is precisely identified by (20). Finally, any exact point $\mathbf{p}_i$ on the cylinder will suffice to determine the radius as $r = |\,(\mathbf{p}_i - \mathbf{p}_*) \times \mathbf{a}\,|$.

7 Analysis of solution reliability

For the vector norm $\|\mathbf{v}\|_p = (|v_1|^p + \cdots + |v_n|^p)^{1/p}$, the subordinate norm of the 9×9 matrix $\mathbf{M}$ in (13) is specified [9] as

$$\|\mathbf{M}\|_p \,=\, \max_{\mathbf{v}\neq\mathbf{0}} \frac{\|\mathbf{M}\mathbf{v}\|_p}{\|\mathbf{v}\|_p}\,,$$

and the p–norm *condition number* $C_p(\mathbf{M})$ of $\mathbf{M}$ is defined by

$$C_p(\mathbf{M}) \,=\, \|\mathbf{M}\|_p\, \|\mathbf{M}^{-1}\|_p\,.$$

If a perturbation $\delta\mathbf{r}$ is imposed on the right–hand–side vector $\mathbf{r}$ in (13), that incurs a corresponding perturbation $\delta\mathbf{v}$ in the solution vector $\mathbf{v}$, the relative errors $\epsilon_{\mathbf{v}} = \|\delta\mathbf{v}\|_p/\|\mathbf{v}\|_p$ and $\epsilon_{\mathbf{r}} = \|\delta\mathbf{r}\|_p/\|\mathbf{r}\|_p$ satisfy

$$\epsilon_{\mathbf{v}} \,\le\, C_p(\mathbf{M})\, \epsilon_{\mathbf{r}}\,. \tag{22}$$

The bound (22) is *sharp*, i.e., it holds with equality for *some* perturbation $\delta\mathbf{r}$. In the cases $p = 1$ and ∞, $\|\mathbf{M}\|_p$ is the greatest of the column and row sums of absolute values of the matrix elements, respectively [9]. Since $\mathbf{M}$ and $\mathbf{M}^{-1}$ are symmetric, $\|\mathbf{M}\|_1 = \|\mathbf{M}\|_\infty$, $\|\mathbf{M}^{-1}\|_1 = \|\mathbf{M}^{-1}\|_\infty$, so $C_1(\mathbf{M}) = C_\infty(\mathbf{M})$, and we may simply write $C(\mathbf{M})$. The condition number gives a (worst–case) indication of the influence of round–off error amplification when the system (13) is solved using floating–point arithmetic.

In the present context, a different source of inaccuracy may be dominant when solving (13). Namely, the elements (15) and (16) of both the matrix $\mathbf{M}$ and right–hand side vector $\mathbf{r}$ are not known exactly, since they are computed from the basis functions (14) evaluated at the data points (x_i, y_i, z_i), whose precision is limited by the accuracy of the OCT distance measurements ρ_i.

To assess the influence of the finite accuracy of the distances ρ_i, they are assumed to have Gaussian (normal) distributions [14] of the form

$$f(\rho_i) \,=\, \frac{1}{\sqrt{2\pi}\,\sigma}\, \exp\left[-\,\frac{(\rho_i - \bar\rho_i)^2}{2\,\sigma^2}\right]\,, \tag{23}$$

where it is assumed that the nominal distance measurements are reasonable estimates of their individual means $\bar\rho_i$, and the same standard deviation $\sigma =$ 0.0005 mm holds for each measurement — this corresponds to $\sim 68\%$ of the measured distances ρ_i being within ± 0.0005 mm of $\bar\rho_i$. We then perform a

Monte Carlo experiment, in which each individual ρ_i is randomly perturbed to a new value $\tilde{\rho}_i$ in accordance with the probability distribution (23). New point coordinates $(\tilde{x}_i, \tilde{y}_i, \tilde{z}_i)$ are then computed from the $\tilde{\rho}_i$ values using (12), and the corresponding matrix elements $\widetilde{M}_{jk}$ and right–hand–side values $\tilde{r}_j$ are obtained from (15) and (16). Solving the resulting linear system $\widetilde{\mathbf{M}}\,\tilde{\mathbf{v}} = \tilde{\mathbf{r}}$, for the resulting perturbed coefficients $\tilde{\mathbf{v}} = [\,\tilde{a}\ \tilde{b}\ \tilde{c}\ \tilde{f}\ \tilde{g}\ \tilde{h}\ \tilde{l}\ \tilde{m}\ \tilde{n}\,]^T$, we define their relative error as

$$\epsilon_{\mathbf{v}} \,=\, \frac{\|\tilde{\mathbf{v}} - \mathbf{v}\|_2}{\|\mathbf{v}\|_2}\,.$$

The Monte Carlo experiment is repeated several times, with different random samplings of the distributions (23), to assess the overall consistency and range of variation in the $\epsilon_{\mathbf{v}}$ values obtained. The examples presented below indicate that this approach offers a more realistic assessment of the accuracy of the computed quadric surface coefficients.

8 Computed examples

The following examples describe results obtained from an implementation of the methodology in the `C` programming language on representative test data sets (all dimensions are in mm). In the conversion (12) of the "raw" OCT probe data to Cartesian coordinates, the cone beam angle is $\phi = 60°$ and the scans are made at azimuthal angle increments $\delta\theta = 0.5°$ for each fixed probe extension δz.

8.1 Example 1

In this example, the cylinder has radius $r = 0.75$, and the axis is specified by the point $\mathbf{p}_* = (x_*, y_*, z_*) = (1.0, 4.0, 0.0)$ and the unit vector $\mathbf{a} = (\lambda, \mu, \nu) = (-0.17364818, -0.33682409, 0.92541658)$. Scans are made at three successive extensions δz, the distances ρ to the cylinder being detected at the angular increment $\delta\theta$ beginning at θ_0, for a total of n points per scan as follows:

- $\delta z = 0.0$, $\theta_0 = -2.0°$, $n = 52$;
- $\delta z = 1.0$, $\theta_0 = -5.0°$, $n = 57$;
- $\delta z = 2.0$, $\theta_0 = -9.0°$, $n = 65$.

The total number of points is $N = 174$. Table 1 compares the exact cylinder coefficients, computed from (9)–(11) and divided by d, with the least–squares fit values. From (18) we obtain $\mathbf{a} = (-0.17503840, -0.33666708, 0.92521178)$ as the estimated cylinder axis, which makes an angle $0.081015°$ with the exact axis $(-0.17364818, -0.33682409, 0.92541658)$. The axis point $\mathbf{p}_*$, determined from (20) has coordinates $(x_*, y_*) = (1.00064338, 4.00260039)$ — as compared to the exact point $(1.0, 4.0)$. Finally, the cylinder radius computed from (21) is $r = 0.746531$, whereas the exact value is $r = 0.750000$. From the computed coefficients we have values $\gamma = 0.00499410$, $\delta = 0.00000022$ of the invariants (4), in fair agreement with the conditions $\gamma \neq 0 = \delta$ identifying a cylinder. Figure 1 compares the computed cylinder with the exact cylinder.

	exact	least–squares
a	0.06866544	0.06847202
b	0.06276800	0.06266601
c	0.01016722	0.01015567
f	−0.00414103	−0.00413862
g	0.02206865	0.02197726
h	0.01137739	0.01133276
l	−0.05210131	−0.05195083
m	−0.24693097	−0.24668571
n	−0.09965198	−0.09946885
d	1.00000000	1.00000000

Table 1: Comparison of exact and least–squares fit coefficients for Example 1.

The condition number of the matrix $\mathbf{M}$ in this example is $C(\mathbf{M}) = 1.81 \times 10^6$. The Monte Carlo accuracy assessment (described in Section 7) was run 100 times with different random numbers satisfying the Gaussian distribution (23), resulting in values of the fractional error $\epsilon_{\mathbf{v}}$ in the computed coefficients ranging between 0.000096 and 0.001095, with a mean value 0.000508.

Overall, the least–squares fitting procedure (Section 5) and the parameter estimation scheme (Section 6) provide a remarkably accurate estimation of the cylinder geometry, despite the relatively low precision of the measurement data. To demonstrate that the accuracy of the data is the only factor limiting the precision with which the cylinder can be identified, the computation was repeated with ρ values computed in double–precision arithmetic, in lieu of the values with 3 decimal place accuracy used above. This resulted in an angular deviation between the estimated and exact axes of only 0.0000008538°, and

$$(x_*, y_*) \,=\, (1.000000000029, 4.000000000119)\,, \quad r \,=\, 0.749999999795$$

for the coordinates of the axis point $\mathbf{p}_*$ and the cylinder radius r.

8.2 Example 2

The cylinder geometry parameters in Example 2 are identical to those used in Example 3, except that the radius was increased to $r = 1.5$. Three scans were made, corresponding to the values

- $\delta z = 0.0$, $\theta_0 = -15.5°$, $n = 106$;
- $\delta z = 1.0$, $\theta_0 = -20.5°$, $n = 119$;
- $\delta z = 2.0$, $\theta_0 = -26.5°$, $n = 134$.

The total number of points is $N = 359$. Table 2 compares the exact cylinder coefficients, computed from (9)–(11) and divided by d, with the least–squares fit values. From (18) we obtain $\mathbf{a} = (-0.18374332, -0.32542690, 0.92754284)$ as the estimated cylinder axis, which makes an angle 0.880816° with the exact axis $(-0.17364818, -0.33682409, 0.92541658)$. The axis point $\mathbf{p}_*$, determined from (20) has coordinates $(x_*, y_*) = (0.99717264, 3.98746160)$ — as compared to the exact point $(1.0, 4.0)$. Finally, the cylinder radius computed from (21) is $r = 1.522544$, whereas the exact value is $r = 1.500000$. From the computed coefficients we have values $\gamma = 0.00641154$, $\delta = 0.00000007$ of the invariants (4), as compared to the exact conditions $\gamma \neq 0 = \delta$ defining a cylinder. Figure 1 compares the computed cylinder with the exact cylinder.

The condition number of the least–squares matrix in this case is $C(\mathbf{M}) = 1.65 \times 10^5$. The Monte Carlo accuracy assessment was run 100 times with different random numbers satisfying the Gaussian distribution (23), yielding values of the fractional error $\epsilon_{\mathbf{v}}$ in the computed coefficients between 0.000068 and 0.000738, with a mean value 0.000303.

When the computation is repeated with double–precision ρ values, in lieu of the values with 3 decimal place accuracy used above, we obtain an angular deviation between the estimated and exact axes of 0.0000000000°, and

$$(x_*, y_*) \,=\, (0.999999999997, 3.999999999988)\,, \quad r \,=\, 1.500000000018$$

for the coordinates of the axis point $\mathbf{p}_*$ and the cylinder radius r.

	exact	least–squares
a	0.07798243	0.07709279
b	0.07128479	0.07145285
c	0.01154678	0.01159307
f	−0.00470292	−0.00441349
g	0.02506307	0.02517422
h	0.01292116	0.01287786
l	−0.05917077	−0.05927620
m	−0.28043625	−0.28051450
n	−0.11317344	−0.11327718
d	1.00000000	1.00000000

Table 2: Comparison of exact and least–squares fit coefficients for Example 2.

8.3 Example 3

In this example the cylinder geometry parameters are $(x_*, y_*) = (1.0, 4.0)$, $\mathbf{a} = (-0.64278761, -0.26200263, 0.71984631)$, and $r = 0.5$. Three scans were made, corresponding to the values

- $\delta z = 0.0$, $\theta_0 = -24.5°$, $n = 48$;
- $\delta z = 1.0$, $\theta_0 = -42.0°$, $n = 53$;
- $\delta z = 2.0$, $\theta_0 = -59.0°$, $n = 52$.

The total number of points is $N = 153$. Table 3 compares the exact cylinder coefficients, computed from (9)–(11) and divided by d, with the least–squares fit values. From (18) we obtain $\mathbf{a} = (-0.64386222, -0.25900228, 0.71997171)$ as the estimated cylinder axis, which makes an angle 0.182742° with the exact axis $(-0.64278761, -0.26200263, 0.71984631)$. The axis point $\mathbf{p}_*$, determined from (20) has coordinates $(x_*, y_*) = (1.00228517, 4.00163039)$ — as compared to the exact point $(1.0, 4.0)$. Finally, the cylinder radius computed from (21) is $r = 0.507851$, whereas the exact value is $r = 0.500000$. From the computed coefficients we have values $\gamma = 0.00514512$, $\delta = -0.00000002$ of the invariants (4), in fair agreement with the conditions $\gamma \neq 0 = \delta$ characterizing a cylinder.

The condition number of the least–squares matrix $\mathbf{M}$ in this example is $C(\mathbf{M}) = 1.20 \times 10^7$. Using 100 runs of the Monte Carlo accuracy assessment with different random numbers that satisfy the Gaussian distribution (23),

	exact	least–squares
a	0.04224430	0.04195657
b	0.06704637	0.06700938
c	0.03468536	0.03449726
f	−0.01212365	−0.01213370
g	0.01357706	0.01356661
h	0.03330945	0.03307726
l	0.00625029	0.00650214
m	−0.25606182	−0.25598535
n	−0.08761768	−0.08742876
d	1.00000000	1.00000000

Table 3: Comparison of exact and least–squares fit coefficients for Example 3.

values of the fractional error $\epsilon_{\mathbf{v}}$ in the computed coefficients between 0.000110 and 0.001457 were obtained, with a mean value 0.000557. As in the preceding examples, essentially exact cylinder geometry parameters were obtained when the computation was repeated with double–precision ρ values.

9 Real-time implementation

Using a modest 1.1 GHz processor, the execution times for identification of the cylinder from the point coordinate data in Examples 1, 2, and 3 were 0.27, 0.53, and 0.24 ms. Since these examples used $N = 174$, 359, and 153 points, the times are consistent with a linear dependence on N, and constitute only a modest fraction of the overall effort required for real–time implementation. The OCT probe tip emits light pulses of 40 μs duration every 50 μs, inclined at 60° to the probe axis. Within the viewing range, reflection intensity data is acquired along each pulse, up to a few mm from the probe tip. The probe rotates along its axis at a 10 Hz rate, and its tip also executes a reciprocating motion along the probe axis at a speed $\sim$ 1–5 mm/s. These motions result in a helical scanning pattern on the target surface.

For a signal of width $\sim 30°$ the probe requires just under 10 ms to trace the scan curve, with sequential scans at 100 ms apart. Further computations are needed to convert the raw OCT data into point coordinates, and a target computation time of 100–200 ms per image frame is anticipated. A "rolling" solution to frame updating may also be used, in which overlapping sequences of scans are used to provide a higher image refresh frequency.

10 Closure

A methodology for real–time identification of the position, orientation, and size of blood vessels, based on discrete distance measurements from an optical coherence tomography (OCT) probe, has been developed and verifed through implementation. The method is sufficiently fast and robust to provide needle guidance for venipuncture procedures through a visual display.

Modelling the blood vessel as a right circular cylinder, the procedure first performs a least–squares fit to the OCT data, in terms of a general quadric surface represented by a symmetric 4×4 matrix. An analysis of the structure of this matrix then allows the right circular cylinder "closest" to the general quadric to be identified. This avoids the need for iterative non–linear surface fitting, which can be computationally demanding, and lacks robustness when methods to identify good starting approximations are not available.

The computed examples show that the cylinder identification procedure is fast, with a computing time that grows only linearly with the total number N of data points, and the cylinder geometry parameters are identified with a high degree of robustness. The method should be adaptable to identification of other simple morphologies, e.g., general quadrics or toroidal surfaces.

Acknowledgement

This work was supported in part by National Science Foundation SBIR Phase II grant 1853242 to WestFace Medical.

Declaration of interests

Conflicts of Interest: The authors certify that no conflicts of interest were incurred in the conduct of the research described herein.

Funding: This work was supported in part by National Science Foundation SBIR Phase II grant 1853242 to WestFace Medical.

Ethics: No ethical issues were incurred in conducting the research described herein.

References

[1] W. Drexler and J. G. Fujimoto (2008), State–of–the–art retinal optical coherence tomography, *Prog. Retin. Eye Res.* **27** (1), 45–88.

[2] L. P. Eisenhart (1939), *Coordinate Geometry*, Dover Publications, Mineola NY (reprint).

[3] R. T. Farouki, C. A. Neff, and M. A. O'Connor (1989), Automatic parsing of degenerate quadric surface intersections, *ACM Trans. Graphics* **8**, 174–203.

[4] A. F. Fercher (1996), Optical coherence tomography, *J. Biomed. Opt.* **1** (2), 157–173.

[5] M. L. Gabriele, G. Wollstein, H. Ishikawa, L. Kagemann, J. Xu, L. S. Folio, and J. S. Schuman (2011), Optical coherence tomography: history, current status, and laboratory work, *Invest. Ophthalmol. Vis. Sci.* **52** (5), 2425–2436.

[6] W. Geitzenauer, C. K. Hitzenberger, and U. M. Schmidt–Erfurth (2010), Retinal optical coherence tomography: past, present, and future perspectives, *Brit. J. Ophthalmol.* **95**, 171–177.

[7] M. R. Hee, J. A. Izatt, E. A. Swanson, D. Huang, J. S. Schuman, C. P. Lin, C. A. Puliafito, and J. G. Fujimoto (1995), Optical coherence tomography of the human retina, *Arch. Ophthalmol.* **113** (3), 325–332.

[8] D. Huang, E. A. Swanson, C. P. Lin, J. S. Schuman, W. G. Stinson, W. Chang, M. R. Hee, T. Flotte, K. Gregory, C. A. Puliafito, and J. G. Fujimoto (1991), Optical coherence tomography, *Science* **254** (5035), 1178–1181.

[9] G. M. Phillips and P. J. Taylor (1973), *Theory and Applications of Numerical Analysis*, Academic Press, London.

[10] D. D. Sampson, P. Andersen, T. van Leeuwen, and R. Wang (2017), Commemorating 25 years of optical coherence tomography: A perspective on biomedical applications, *J. Biomed. Opt.* **22** (12), 1–2.

[11] V. Snyder and C. H. Sisam (1914), *Analytic Geometry of Space*, Henry Holt & Co., New York.

[12] D. M. Y. Sommerville (1951), *Analytical Geometry of Three Dimensions*, Cambridge University Press.

[13] J. V. Uspensky (1948), *Theory of Equations*, McGraw–Hill, New York.

[14] H. D. Young (1962), *Statistical Treatment of Experimental Data*, McGraw Hill, New York.

Figures

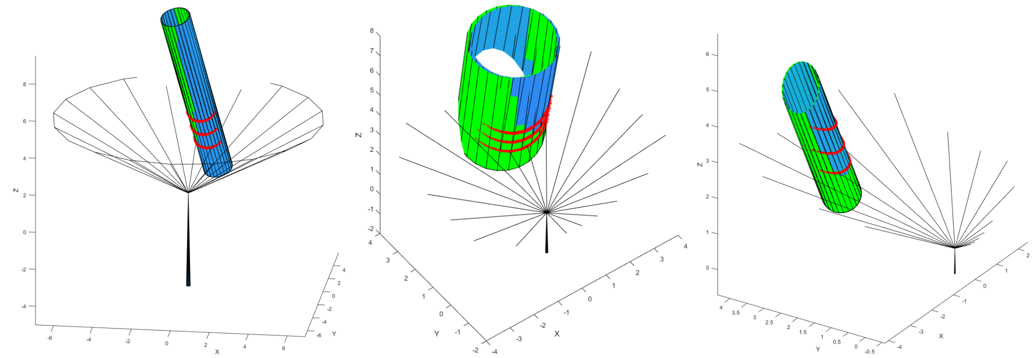

Figure 1: Cylinders identified from the OCT probe data (red) using 3 scans with a total number of 174 points in Example 1 (left), 359 points in Example 2 (center), and 153 points in Example 3 (right). The exact cylinder is shown in blue, and the computed cylinder is shown in green.